THE JOURNAL OF PHYSICAL CHEMISTRY C

Article

pubs.acs.org/JPCC

# Determination of Complete Melting and Surface Premelting Points of Silver Nanoparticles by Molecular Dynamics Simulation

H. A. Alarifi,[†] M. Atiş,[‡] C. Özdoğan,[§] A. Hu,*[,†] M. Yavuz,[†,§] and Y. Zhou[†]

[†]Department of Mechanical and Mechatronics Engineering, Centre for Advanced Material Joining, University of Waterloo, 200 University Avenue West, Waterloo, Ontario N2L 3G1, Canada

[‡]Department of Physics, Nevsehir University, 2000 Evler, 50300 Nevsehir, Turkey

[§]Department of Materials Science and Engineering, Çankaya University, Yenimahalle, 06810 Ankara, Turkey

Supporting Information

**ABSTRACT:** A molecular dynamics simulation based on the embedded-atom method was conducted at different sizes of single-crystal Ag nanoparticles (NPs) with diameters of 4 to 20 nm to find complete melting and surface premelting points. Unlike the previous theoretical models, our model can predict both complete melting and surface premelting points for a wider size range of NPs. Programmed heating at an equal rate was applied to all sizes of NPs. Melting kinetics showed three different trends that are, respectively, associated with NPs in the size ranges of 4 to 7 nm, 8 to 10 nm, and 12 to 20 nm. NPs in the first range melted at a single temperature without passing through a surface premelting stage. Melting of the second range started by forming a quasi-liquid layer that expanded to the core, followed by the formation of a liquid layer of 1.8 nm thickness that also subsequently expanded to the core with increasing temperature and completed the melting process. For particles in the third range, the 1.8 nm liquid layer was formed once the thickness of the quasi-liquid layer reached 5 nm. The liquid layer expanded to the core and formed thicker stable liquid layers as the temperature increased toward the complete melting point. The ratio of the quasi-liquid layer thickness to the NP radius showed a linear relationship with temperature.

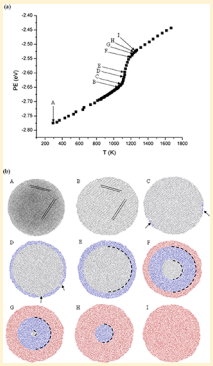

## INTRODUCTION

Fundamental understanding of the thermodynamic properties of Ag nanoparticles (NPs) is important because of their potential utilization in nanoscale devices,[1] wire bonding,[2,3] and development of lead-free soldering materials.[4] It has been shown experimentally and theoretically that NPs melt at temperatures below the melting point of the bulk due to their higher surface energy.[5−11] The liquid drop model,[12] Shi's model,[13] and Hanszen's model[14] are found to be the most popular models for predicting the complete melting point ($T_m$) of NPs. According to Hanszen's model, melting of a NP starts on the surface by the formation of a thin liquid layer at $T_m$ of the NP, which then expands toward the core leading to complete full transition of the structure from solid to liquid. This initial stage of melting is called surface premelting, which reduces the total interfacial energy of the material. The energetic requirement for surface premelting to occur is that the solid−vapor interfacial energy ($\gamma_{sv}$) should be larger than the sum of solid−liquid interfacial energy ($\gamma_{sl}$) and the liquid−vapor interfacial energy ($\gamma_{lv}$).[15] This condition can only be satisfied for Ag NPs and is not the case for either Ag microparticles or the bulk, where surface premelting does not occur.[16]

Surface premelting was experimentally confirmed for Sn,[17,18] Pb,[19] and Pt NPs[20] and has also been numerically confirmed for Au[21] and V NPs[22] and for Cu[23] and Ni nanoclusters.[24,25] An analytical model was recently developed by Cherneyshev to determine the onset temperature of surface premelting ($T_{sm}$) for NPs in terms of the mean-field approximation.[26]

Complete melting points ($T_m$) of Ag NPs obtained experimentally have shown scattered data in the range of 383 to 953 K,[27−32] while the only published molecular dynamics (MD) simulation was performed on very small clusters with 12−14 atoms.[33] Furthermore, the diversity of the analytical models found in literature for determining $T_m$ and the different results obtained from these works certainly makes it difficult to correctly predict $T_m$ of NPs. In this contribution, we have used our own linear scaling parallel MD code[34] to find $T_m$ and $T_{sm}$ for individual single-crystal Ag NPs of sizes ranging from 4 to 20 nm in diameter. Simulation of larger NPs will be considered in future work. Our code has allowed us to utilize multiple processors simultaneously and simulate large sizes of NPs. The current results showed that 8 nm and smaller Ag particles melted homogeneously and $T_m$ values were found to be in good agreement with Shi's model and the liquid drop model. For 8 to 10 nm particles, our results have shown good agreement with Hanszen's model, at which the melting starts by forming a stable liquid layer of critical thickness ($t_o$) that expands to the core as the temperature is increased. Complete melting points of larger NPs have been found to deviate from Hanszen's model due to the formation of a thicker stable liquid layer

**Received:** November 22, 2012
**Revised:** May 16, 2013

 © XXXX American Chemical Society  dx.doi.org/10.1021/jp311541c | J. Phys. Chem. C XXXX, XXX, XXX−XXX

below $T_m$. We also found that the ratio of the thickness of the quasi-liquid layer to the radius of the NP linearly increased as the temperature increased to $T_m$.

## THEORETICAL METHODS

**Computational Methods.** The silver atoms in the NPs were arranged as an FCC-truncated Marks decahedra ($D_h$) that defines planes (111) and (100) as surface facets.[35] The developed linear scaling parallel MD code[34] was used to investigate melting and surface premelting behaviors of the NPs. This code was based on the Voter−Chen version[36] of the embedded-atom method (EAM) potential.[37] Unlike a first-principles method, semiempirical methods such as EAM can be used to simulate large sizes of NPs as well as very small clusters.[38] Simulation of large clusters can only be performed by using semiempirical potentials such as Sutton−Chen,[39] the many-body Gupta,[40] Finnis−Sinclair,[41] the embedded atom[42−46] and related methods,[47−49] and MD simulations.[50−54] We chose the EAM for the generality of its functional, good agreement with experiments and the first-principles calculations and the high computational efficiency that allowed us to simulate relatively large NPs. The EAM was originally developed by Daw and Baskes[55] and parametrized by Voter and Chen[36] by simultaneously fitting the potential to the properties of bulk silver and $Ag_2$. The total energy $E$ of a monatomic system in the EAM potential is represented by

$$E_{tot} = \sum_i F(\bar{\rho}_i) + \frac{1}{2}\sum_{i\neq j} V(r_{ij}) \quad (1)$$

where $V(r_{ij})$ is a pairwise potential as a function of the interatomic distance $r_{ij}$ between atoms $i$ and $j$, $F$ is the embedding energy, and $\bar{\rho}_i$ is the total host electron density at the position of atom $i$ and can be calculated by the following formula

$$\bar{\rho}_i = \sum_{i\neq j} \rho(r_{ij}) \quad (2)$$

where $\rho(r)$ is the density function and can be calculated by the following equation:

$$\rho(r) = r^6[e^{-\beta r} + 2^9 e^{-2\beta r}] \quad (3)$$

where $r$ is the distance between the atoms and $\beta$ is an adjustable parameter. The pairwise potential $V(r)$ based on Morse potential is calculated using the following equation

$$V(r) = D_M[1 - e^{\alpha_M(r-R_M)}]^2 - D_M \quad (4)$$

where $D_M$ is the depth of the potential well, $R_M$ is the interatomic distance at the minimum of the potential well, and $\alpha_M$ is a measure of the curvature of the potential well at its minimum, respectively.

For higher precision, Hamming's modified fourth-order predictor-corrector propagator has been employed with a step size of 2 femtoseconds (fs, $2 \times 10^{-15}$ s), which guarantees the conservation of total energy of a NP within an accuracy range of 0.03 to 0.15% according to our results. The initial velocities of atoms in the NP were assigned according to the Maxwell−Boltzmann distribution at a specific temperature. The NPs were first relaxed at 300 K (room temperature) for 20 ps to achieve equilibration before heating, which was gradually applied by increasing the NP temperature in intervals. This was achieved by multiplying the velocities of atoms by a scaling factor that is calculated as a ratio of the target temperature to the present temperature. Accordingly, the total kinetic energy ($E_k$) of the atoms in the NPs is obtained via the equipartition theorem. The NPs were then equilibrated for 20 ps at each temperature, which was long enough to dampen the fluctuations in temperature. Consequently, the NPs reached the desired temperature at each heating interval in a reliable manner. From this fact, one may argue that the equilibrium averages, which are sensitive to temperature fluctuations, were reasonably taken into consideration. However, we should also point out that we have made use of a simple velocity rescaling scheme to fix the temperature rather than contacting with a heat bath such as the Nosé−Hoover thermostat. Nevertheless, one may argue that the present velocity rescaling scheme has successfully maintained thermodynamic properties in the canonical ensemble averages by applying an appropriate heating rate.

During the heating process, the last phase space point of a calculation was used as an input for the next temperature calculation and the temperature (or $E_k$) and average potential energy (PE) were calculated. Heating of the NPs was then gradually applied by increasing their internal kinetic energies ($E_k$) for 20 ps at each temperature interval. The temperature of the NP was calculated by the following equation:

$$T = \frac{2\langle E_k\rangle}{k(3N-6)} \quad (5)$$

where $E_k$ is the total kinetic energy of the atoms in the NP, $k$ is the Boltzmann constant, and $N$ is the total number of atoms in the NP. The dynamics were monitored by short-time (10 fs) averages of the NP temperature. The short-time average was taken to lower the fluctuation in the kinetic energy (KE) values that occurred due to the flow between the PE and the KE during the oscillation of the atoms around their equilibrium positions. Taking the short-time average is more important at high temperatures as the fluctuations in the KE values become larger.

The heating rate was chosen based on a trade-off between physical reasoning and computational expenses. Although instantaneous heating is computationally less expensive than gradual heating, the system may stick on a local minimum at the potential energy surface (PES). Therefore, we have performed gradual heating on the NPs, and the heating rate was chosen based on a preliminary simulation performed on a 4 nm particle in the range of 325 to 1675 K with 50 K steps leading to a $T_m$ value of ∼875 K. For better accuracy, we reduced the temperature step for all sizes of NPs to 10 K in the range of 825 to 1275 K. The maximum temperature of this range was chosen to be slightly higher than $T_m$ of the bulk (1235 K).

**Analytical Methods.** We compared $T_m$ obtained by MD simulation to those obtained by using the liquid drop model,[12] Shi's model,[13] and Hanszen's model.[14] The liquid drop model assumes that $T_m$ of an NP is primarily based on the variation of the cohesive energy and the surface tension of the NP. According to the liquid drop model, the bulk atomic cohesive energy per coordination number can be related to the melting point of the bulk $T_m(\infty)$ by the following equation

$$a_v = 0.0005736T_m(\infty) + c \quad (6)$$

Also, average cohesive energy per atom of a NP can be related to its complete melting point $T_m(d)$ by the following equation


dx.doi.org/10.1021/jp311541c | J. Phys. Chem. C XXXX, XXX, XXX−XXX

$$a_{v,d} = 0.0005736T_m(d) + c \quad (7)$$

where $c$ is a constant in both equations and $d$ is the diameter of the NP. Average cohesive energy per atom ($a_{v,d}$) of a NP can be directly related to cohesive energy of the bulk ($a_v$), atomic volume ($v_o$), and the solid−vapor interfacial energy ($\gamma_{sv}$) by the following equation:

$$a_{v,d} = a_v - \frac{6v_o\gamma_{sv}}{d} \quad (8)$$

Equation 8 shows that cohesive energy per atom decreases as the size of the NP decreases and the rate of the decrease depends on the atomic volume ($v_o$) and the solid−vapor interfacial energy ($\gamma_{sv}$). By replacing the values of the cohesive energies in eq 8 by the values of the complete melting points from eqs 6 and 7, we get

$$T_m(d) = T_m(\infty)\left(1 - \frac{6v_o\gamma_{sv}}{0.0005736dT_m(\infty)}\right) \quad (9)$$

where $T_m(d)$ and $T_m(\infty)$ are complete melting points of the NP and the bulk; respectively. Equation 9 was modified to eq 10 by introducing a dimensional parameter $\beta$ that depends on $v_o$ and $\gamma_{sv}$

$$T_m(d) = T_m(\infty)\left(1 - \frac{\beta}{d}\right) \quad (10)$$

where melting point of bulk Ag is 1235 K and $\beta$ is estimated as 0.96564 nm.[12]

We have also considered Shi's model,[13] which was based on Lindemann's criterion[56] to find the complete melting point of the NPs. Lindemann's criterion suggested that an NP melts when the root-mean-square displacement (msd) of the atoms exceeds a certain fraction of the interatomic distance. Shi specified $T_m$ based on the average msd value of both the bulk and surface atoms and can be calculated by the following equation

$$T_m(d) = T_m(\infty)\exp\left[-(\alpha - 1)/\left(\frac{d}{2r_o} - 1\right)\right] \quad (11)$$

where $r_o$ is the NP radius at which all atoms are located at the surface and $\alpha$ is a material constant that can be calculated by the following equation

$$\alpha = \frac{2S_{vib}(\infty)}{3R} + 1 \quad (12)$$

where $S_{vib}(\infty)$ is a vibrational component of melting entropy (= 7.98 J/mol K for bulk Ag)[57] and $R$ is the ideal gas constant (= 8.314 J/mol K); this will give $\alpha$ = 1.64. The value of $r_o$ is equal to $3h$, where $h$ is the height of a monolayer of atoms on the bulk crystal surface. The value of $h$ is equal to $a/2$ for FCC material, where $a$ is the lattice constant ($a$ = 0.409 nm for Ag). This will give $r_o$ as 0.6135 nm for Ag.

We have also considered Hanszen's model for finding $T_m$ of a NP.[14] Hanszen assumed that $T_m$ and $T_{sm}$ are equal and the melting process starts at the surface of the NP by forming a liquid layer of a given critical thickness ($t_o$) around the solid core at $T_m$ of the NP. Any infinitesimal increase in the temperature above $T_m$ destroys the equilibrium between the liquid layer and the solid core, and the liquid layer would expand into the solid core of the NP. According to Hanszen's model, the complete melting point of a NP can be determined by the following equation

$$T_m(d) = T_m(\infty) - \frac{2T_m(\infty)}{Q}\left[\frac{\gamma_{sl}}{\rho_s\left(\frac{d}{2} - t_o\right)} + \left(\frac{2\gamma_{lv}}{d} + \frac{\Delta P}{2}\right)\left(\frac{1}{\rho_s} - \frac{1}{\rho_l}\right)\right] \quad (13)$$

where $Q$ is the latent heat of fusion of the bulk, $t_o$ is the critical thickness of the liquid layer, $\gamma_{sl}$ and $\gamma_{lv}$ are the bulk interfacial energy between solid−liquid and liquid−vapor, respectively, $\rho_s$ and $\rho_l$ are the densities of solid and liquid, respectively, $\Delta P$ is the difference between the vapor pressure of a flat liquid surface ($r = \infty$) at $T_m(\infty)$ and the vapor pressure at the surface of a liquid shell with an outer radius $r$ at $T_m(d)$. By substituting the following values of Ag variables into eq 13, $Q = 1.06 \times 10^9$ erg/g, $\gamma_{sl}$ = 184 dyn/cm, $\gamma_{lv}$ = 910 dyn/cm, $\rho_s$ = 10.49 g/cm$^3$, and $\rho_l$ = 9.35 g/cm$^3$ ($\Delta P$ can be ignored for Ag),[58] we get the following simplified equation

$$T_m(d) = T_m(\infty) - 2463\left(\frac{1}{0.603\left(\frac{d}{2} - t_o\right)} - \frac{2}{d}\right) \quad (14)$$

The theoretical surface premelting point ($T_{sm}$) was calculated by the following equation that was developed by Chernyshev[26]

$$T_{sm}(d) = \left(\frac{3}{4}\alpha\right)^{-1}\{1 + y(d)\}\exp[-y(d)]T_m(\infty) \quad (15)$$

where $y(d)$ is a function that can be calculated by eq 16.

$$y(d) = \frac{(\alpha - 1)}{\left(\frac{d}{2r_o} - 1\right)} \quad (16)$$

Chernyshev developed the model based on Shi's model and has shown that surface premelting does not take place if the NP radius is smaller than a critical radius $r_c$, which is different for different materials. Instead, the surface layer makes a transition to a pseudocrystalline state before the whole particle melts.[59]

## RESULTS AND DISCUSSION

Figure 1a shows the relationship between average PE of atoms in the NPs versus temperature for an 18 nm particle. It can be clearly seen that the PE curve passed through three stages. In the first stage, a gradual increase in the PE was seen between points A (292 K) and C (1086 K) as the temperature of the NP increased. The second stage started at point C and ended at point I (1251 K) with a higher rate of increase than the first stage within a shorter range of temperatures. The third stage started at point I, at which the slope of the PE curve decreases but is still slightly higher than the slope of the first stage. Figure 1b shows the atomic arrangement of the NP at different temperatures by cutting a cross section at the center of the NP with a thickness of three atomic layers (0.6 nm), which is enough to identify the crystallographic planes across the NP. By relating the PE curve to the cross-sectional images of the NP, the crystallographic planes were found to be clear through the NP during the first stage of the curve, indicating a solid phase. Point C is the beginning of the second stage at which amorphous regions started to appear on the surface, as


dx.doi.org/10.1021/jp311541c | J. Phys. Chem. C XXXX, XXX, XXX−XXX

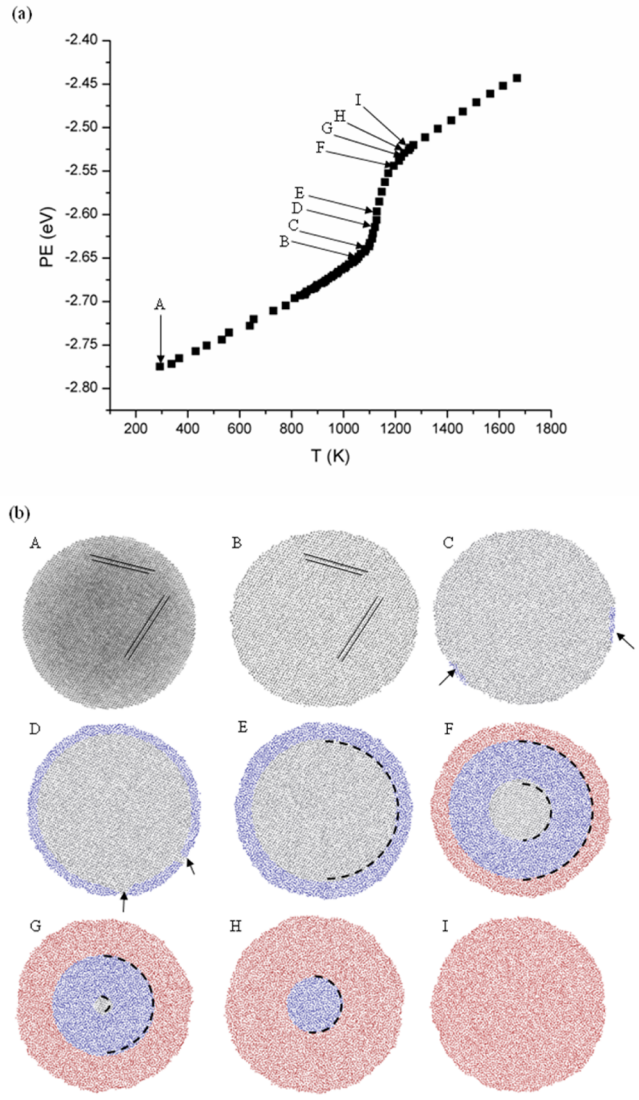


**Figure 1.** (a) Potential energy (PE) values during heating of 18 nm Ag particle. (b) Atomic arrangement of the 18 nm Ag particle at different temperatures indicated by letters on the PE curve. Atoms are represented by dots. The lines in the atomic plots of points A and B represent the orientations of the crystallographic planes. Arrows on plot C point toward quasi-liquid ponds. Arrows at plot D point toward solid regions at the surface. Each color in the atomic plots represent a phase (gray: solid, blue: quasi-liquid, red: liquid), and the dashed arcs represent the interfaces between these phases.

indicated by arrows. These regions are amorphous because the atomic coordinator does not display any long-range orders with them. As provided in literature, we determine an amorphous region as a quasi-liquid phase if their transport properties are between solid and liquid. As further discussed below in the discussion of Figures 2 and 3, the identification of the liquid and the quasi-liquid phases was based on PE and KE plots of the surface layers. These quasi-liquid ponds grew and coalesced as the temperature increased to point D (1021 K), at which a nearly full quasi-liquid layer was formed except for small regions indicated by arrows. A contiguous quasi-liquid layer of 1.9 nm thickness was formed at point E (1128 K) and reached a thickness of 5 nm as the temperature increased to F (1193 K). At this point, the outer 1.8 nm layer converted into liquid while the rest of the amorphous layer remained in the quasi-liquid

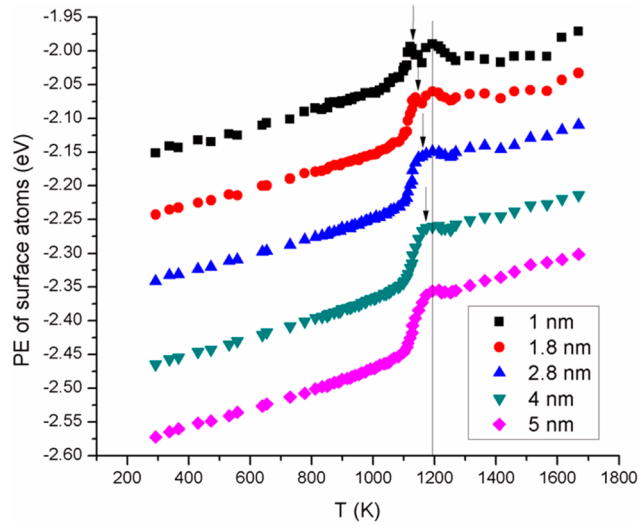


**Figure 2.** Potential energy (PE) values of the outer layer of 18 nm particle with different thicknesses during the heating process. The arrows show the temperature at which the layer transits to the quasi-liquid phase. The vertical line shows the point at which the 1.8 nm liquid layer is formed.

phase. 1.8 nm is the minimum thickness that can be considered as a liquid and is equal to about nine atomic layers, where the thickness of a single atomic layer is equal to half of the lattice parameter for FCC material.[13] Both liquid and quasi-liquid layers expanded to the core and completed the melting process as the temperature increased toward points G (1222 K), H (1234 K), and I (1251 K), which stands for the end of the second stage on the PE curve. Because the PE is an average value of all atoms, we have attributed the dramatic increase in the PE values during the second stage to the continuous conversion of solid-like atoms to quasi-liquid like atoms and then to liquid-like atoms. Therefore, $T_{sm}$ and $T_m$ of NPs have been determined at the temperature at which the PE or KE dramatically changed its slope.

Figure 2 shows the average PE of surface atoms of the outermost layers of the 18 nm particle during heating. These curves showed a similar trend to the average PE of all atoms in Figure 1 except for the second stage. The outer 1 and 1.8 nm surface layers showed two peaks in the melting stage. The first corresponds to the transition of the layer from solid to a quasi-liquid phase, while the second indicates transition to a liquid. The decrease in PE values after reaching these peaks has been interpreted as being due to the conversion of the PE to KE instantaneously after phase transition. These two peaks merged into a single kink once the thickness of the quasi-liquid layer reached 5 nm and the outer 1.8 nm layer converted to liquid.

Figure 3 shows the average KE of atoms in each 0.2 nm layer starting from center to surface of an 18 nm particle at different temperatures during melting. The Figure is divided horizontally into different phases. Only KE values of outer layers that showed stable states in the temperature range of 1114 to 1213 K were plotted while the KE values of the inner unstable layers were eliminated from the plot. KE values of these unstable layers did not display a minimum (a stable state) prior to transition to quasi-liquid phase and therefore they resided in the quasi-liquid region although they were solid. At 1127 K, the KE values of outer layers started to increase and transit to the quasi-liquid regions. Although the temperature of the NP was increased by increasing the total KE of all atoms, as shown in eq


dx.doi.org/10.1021/jp311541c | J. Phys. Chem. C XXXX, XXX, XXX−XXX

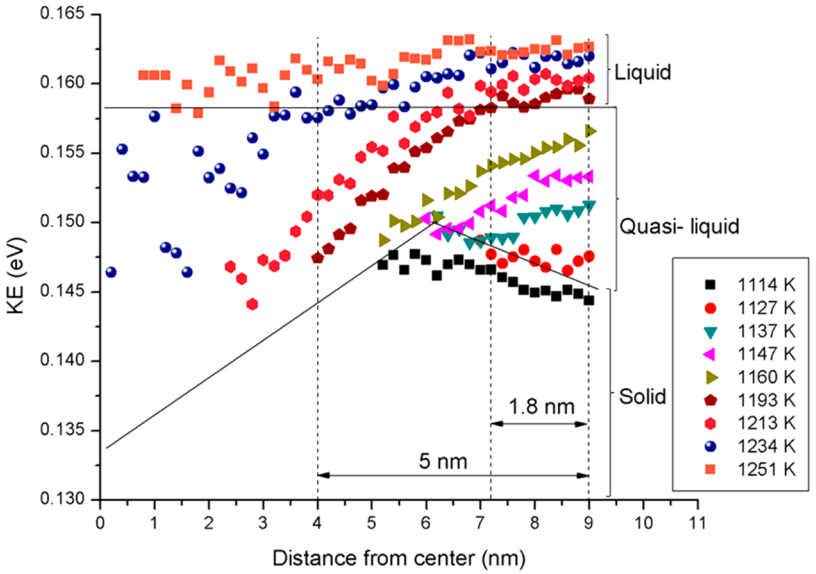


**Figure 3.** Average kinetic energy (KE) of atoms in each 0.2 nm layers of 18 nm particles at different temperatures. The lines show the borders between different phases. Error bars were eliminated due to their interference with the average value of KE of other temperatures.

5, only KE of outer layers increased, and the heat was not transferred to the inner layers. This can be attributed to free vibration of the surface atoms and the larger bond length between atoms at the inner layers.[60] The Figure shows that the thickness of the quasi-liquid layer increased as the temperature increased to 1160 K. At 1193 K (point F in Figure 1), which is the same temperature of the second peak in Figure 2, the quasi-liquid layer thickness reached 5 nm and the outer 1.8 nm layer became constant as an indication of forming the first liquid layer with critical thickness ($t_o$ = 1.8 nm). The 5 nm can thus be considered as the minimum thickness of a quasi-liquid layer that allows the outer 1.8 nm layer to transit to liquid without having a high interfacial energy with the solid core. The thickness of the liquid layer increased as the temperature increased and completed the melting process at 1251 K (point I in Figure 1), which is higher than $T_m$ of the bulk (1234 K). As it will be discussed below, slower heating rate would reduce $T_m$ of the 18 nm particle to 1210 K.

Figure 4 shows the relationship between the thicknesses of quasi-liquid and liquid layers during the heating process. In the range of temperatures between 1086 and 1128 K (points C and E in Figure 1), quasi-liquid ponds were formed on the surface. The first contiguous quasi-liquid layer was of 1.9 nm thickness and was formed at 1128 K (point E in Figure 1), as indicated by the arrow on the Figure. The first formed liquid layer was of 1.8 nm thickness and was formed at 1193 K (point F in Figure 1), at which the quasi-liquid layer reached 5 nm thickness. As shown in the Figure, the increase in the thicknesses of the quasi-liquid and liquid layers could be fitted by parabolic curves.

Figure 5 shows the average PE of the atoms in the NP versus temperature for different sizes of Ag NPs. PE curves passed through the three stages previously explained in Figure 1 with increasing PE values as the NP size decreased. The second stage of the PE curve for 7 nm and smaller particles showed a vertical increase in the PE. This means that $T_{sm}$ and $T_m$ are equal and surface premelting did not occur for these NPs. This confirms the previous theoretical studies that suggested that surface premelting does not take place if the radius of the NP is smaller than a critical radius ($r_c$) (3.62 nm for Ag).[59] We have also observed that melting of smaller NPs started by forming

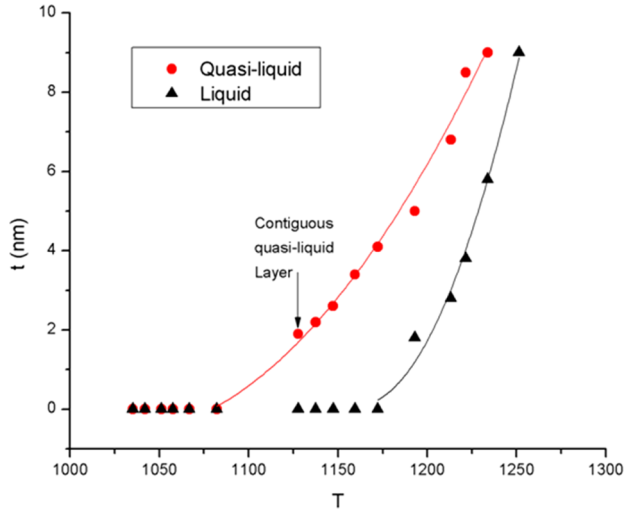


**Figure 4.** Thicknesses of quasi-liquid and liquid layers during the heating process of 18 nm particle. The arrow points to the first contiguous quasi-liquid layer. The curves show parabolic fit of thicknesses of quasi-liquid and liquid layers.

quasi-liquid regions on the surface, which expanded toward the core, as shown in Figure 6b for a 6 nm particle. The atomic plots were obtained by showing three atomic planes at the center of the NPs at different temperatures. Unlike larger particles, quasi-liquid and liquid layers did not reach equilibrium with the solid core and expanded toward inner atoms to complete melting at one temperature, as shown by the PE values in Figure 6a.

Figure 7 shows the average KE of atoms in each 0.2 nm layer starting from the center of the NP toward the surface at the temperature at which the liquid layer was formed. Horizontal lines correspond to the minimum KE of liquid atoms. The thickness of the liquid layer formed on the 20 nm particle was 1.8 nm, and this was found to apply to other NPs in the size range of 8 to 18 nm. The thickness of the quasi-liquid layer that allowed the outer 1.8 nm to transit to liquid was found to be 5 nm, and this applied to the size range of 12 to 20 nm and was


dx.doi.org/10.1021/jp311541c | J. Phys. Chem. C XXXX, XXX, XXX−XXX

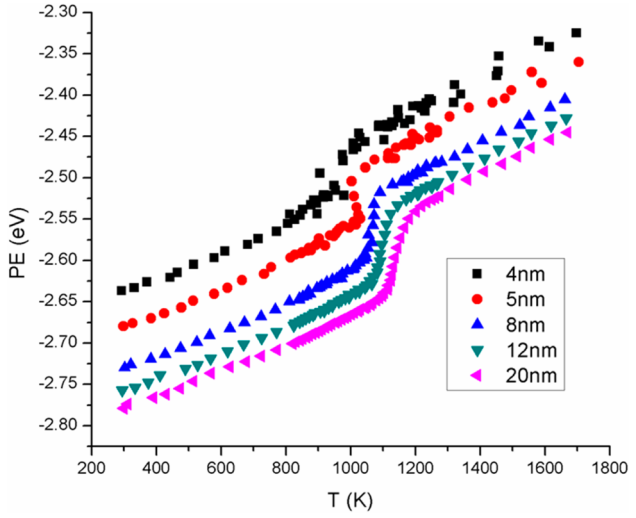


**Figure 5.** Potential energy (PE) values of different sizes of Ag nanoparticles during the heating process.

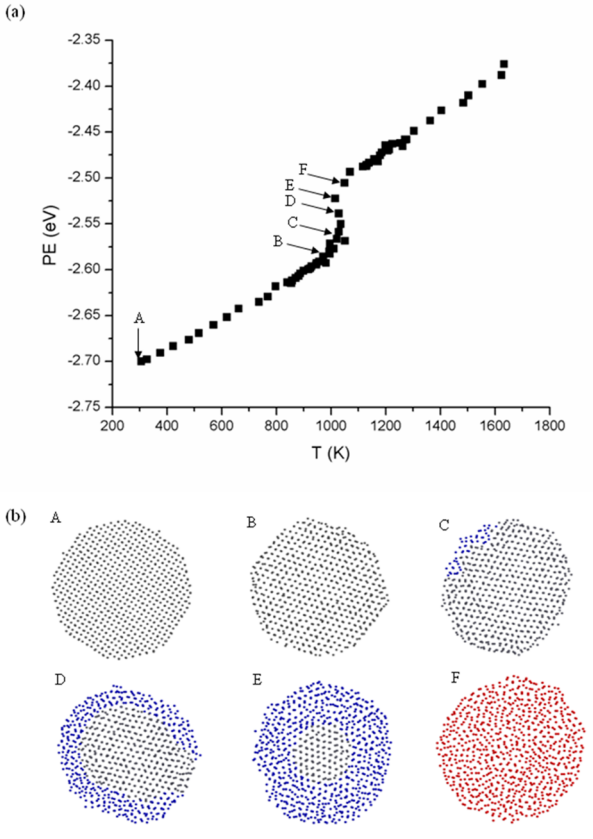


**Figure 6.** (a) Potential energy (PE) values during heating of 6 nm Ag particle. (b) Atomic arrangement of the 6 nm Ag particle at different temperatures shown by letters on the PE curve. Atoms are represented by dots. Each color in the atomic plots represents a phase (gray: solid, blue: quasi-liquid, red: liquid).

equal to radius of the NP for 8 to 10 nm particles. KE values of 4 and 6 nm particles showed a constant value, which is evidence of melting at a single temperature.

As shown in Figure 8, the ratio of quasi-liquid shell thicknesses to the NP radius was found to have a linear relationship with temperature during the surface premelting stage. The slope of the relationship moved toward a vertical line

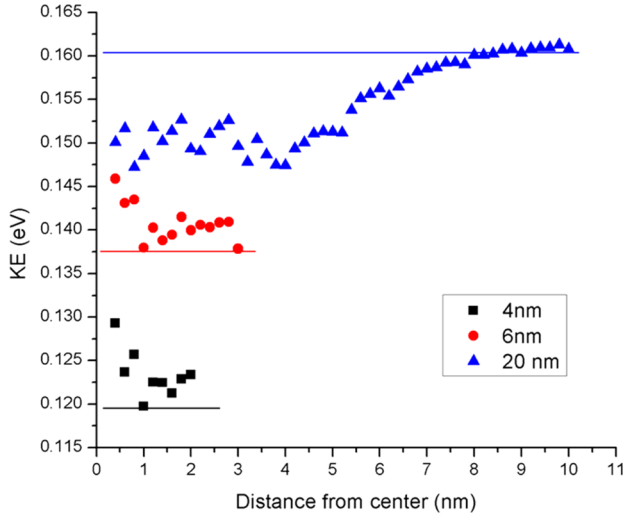


**Figure 7.** Average kinetic energy (KE) of atoms in each 0.2 nm layer for different sizes of nanoparticles at the temperature at which the liquid layer forms at the surface. The horizontal lines show the border between liquid and quasi-liquid regions at each size. Error bars were eliminated due to their interference with the average value of KE of other temperatures.

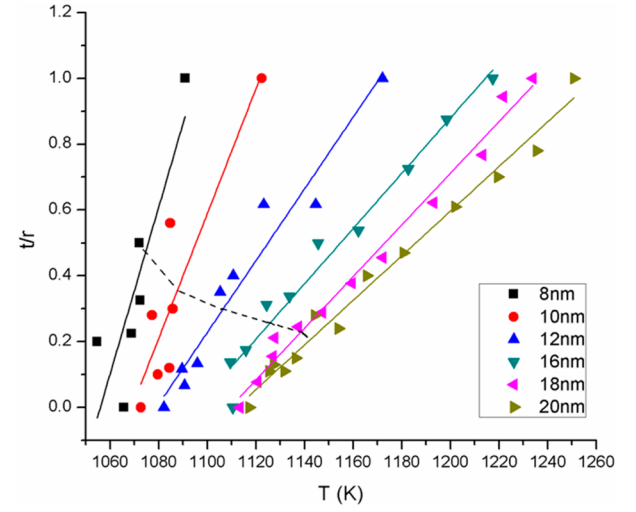


**Figure 8.** Relationship between the ratio of the quasi-liquid layers thickness to the radius of the nanoparticle and temperature. The lines show a linear fit of the data at each nanoparticle size. The dashed line intercepts the data at the critical thickness (to = 1.8 nm).

within a shorter temperature range as the NP size decreased to 8 nm, the minimum size at which the surface premelting occurred. The Figure shows that the quasi-liquid layers were stable and in equilibrium with the solid core. Further increase in temperature broke this equilibrium, and the thickness of the quasi-liquid layers increased as the temperature of the NP increased. These equilibrium points did not exist for particles smaller than 8 nm. Instead, the whole particle melted at a single temperature.

Complete melting points ($T_m$) and surface premelting points ($T_{sm}$) obtained by our simulation are compared with the theoretical models in Figure 9. Surface premelting points ($T_{sm}$) showed values lower than $T_m$ for 8 nm and larger particles, and the gap between $T_m$ and $T_{sm}$ increased as the NPs size increased. Figure 9 also shows that surface premelting did not


dx.doi.org/10.1021/jp311541c | J. Phys. Chem. C XXXX, XXX, XXX−XXX

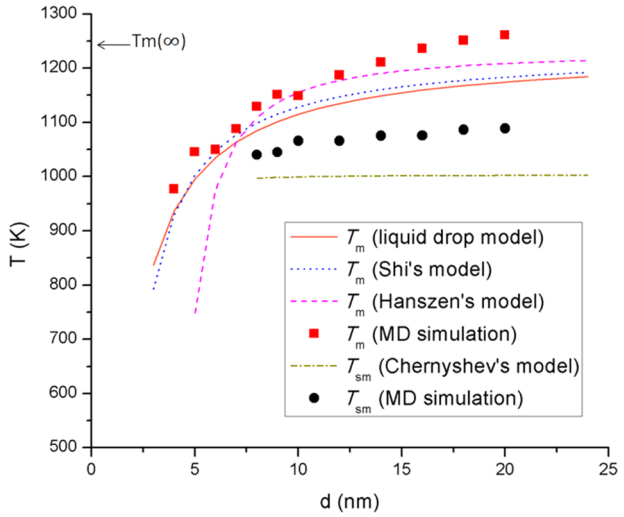


**Figure 9.** Melting points ($T_m$) and surface premelting points ($T_{sm}$) of different sizes of Ag nanoparticles determined by our simulation and by the other theoretical models.

occur for NPs smaller than 8 nm. Complete melting point values obtained by our simulation are in good agreement with the liquid drop model and Shi's model for NPs smaller than 8 nm and with Hanszen's model for 8, 9, and 10 nm particles. Complete melting points of larger NPs started to deviate from Hanszen's model and approached $T_m$ of the bulk.

The liquid drop model and Shi's model have ignored the effect of the formation of a liquid shell in their equations and assumed homogeneous melting of the NPs without passing through the surface premelting stage. This is the reason behind the agreement between both models and our results for NPs that are smaller than 8 nm because we found no surface premelting at those smaller particles. For 8 nm and larger particles, our results showed higher complete melting points than those expected by both models. Previous experimental results of relatively large Pb, Sn, In, and Bi NPs of sizes in the range of (6 to 20 nm) have also shown higher complete melting points than the liquid drop model,[61] and the reason for this was suggested to be the substrate effect on the complete melting point of the NPs.[12] However, our work shows that the formation of the liquid shell and its effect on the heat transfer within the NP might be another significant reason behind this difference.

Hanszen's model was based on classical laws of thermodynamics and assumed that the melting process begins by forming a thin liquid layer on the surface of the NP. The physical parameter of the liquid layer and the interfacial energies between this liquid layer and both vapor and solid core were introduced in eq 13. This is the reason behind the agreement between our results and Hanszen's model for NPs in size range of (8 to 10 nm) and the disagreement for smaller particles on which a liquid shell does not form prior to melting. The critical thickness ($t_o$) of the liquid layer is introduced in eq 14 and can be identified by finding the best fit between $T_m$ obtained by eq 14 and by our simulation. This is the minimum thickness at which the amorphous layer can be considered as liquid; thinner layers are considered as quasi-liquid layers.[62] The best fit of $T_m$ determined by our simulation and by eq 14 is at a critical thickness ($t_o$ = 1.8 nm), which is the same critical thickness obtained from KE plots in Figure 7. Previous experimental work identified the critical thickness of Ag as 1.01[58] and 2 nm.[63]

Complete melting points ($T_m$) of NPs that are larger than 10 nm started to deviate from Hanszen's model and approached $T_m$ of the bulk due to the formation of multiple liquid layers during the melting stages. This is different from Hanszen's assumption that suggested that only one liquid layer of critical thickness ($t_o$) is formed prior to melting and further increase in temperature would lead to a complete melting of the NP without passing through other equilibrium states. However, our work agrees with another study that showed that surface premelting of Pb occurred at broad range of temperatures and the thickness of the liquid layer increased as the temperature increased.[64]

The only reported relationship between $T_{sm}$ and the size of the NP was the theoretical model developed by Chernyshev.[26] This model defined $T_{sm}$ as the temperature at which liquid ponds started to form on the surface of the NP. Figure 9 shows that $T_{sm}$ values obtained by Chernyshev for Ag NPs of sizes between 8 and 20 nm have nearly a constant value of 1000 K. $T_{sm}$ obtained by our simulation are higher and increased from 1072 K for an 8 nm particle to 1144 K for 20 nm particle. Unlike Hanszen's model, Chernyshev's model has not considered the quasi-liquid state of the surface atoms.

Figure 10 shows the freezing process of 4 nm Ag particle and melting of the formed polycrystalline particle. Figure 10a shows the PE values of the heating process of the original single-crystal NP, followed by cooling and reheating. Atomic arrangements of three atomic planes at the center of the NP during the cooling and reheating process are plotted in Figure 10b. Plot A shows the particle in the liquid state at (1698 K), which is the last temperature of the first heating process of the single-crystal particle and the starting point of the cooling process. The NP remained in the liquid phase at point B (683 K) and started to freeze at point C (663 K) by forming the surface facets of the NP. The freezing process occurred at a range of temperatures and ended by forming a polycrystalline configuration at point E (470 K). The slope of the PE values increased during the freezing process due to continuous conversion of liquid-like atoms to solid-like atoms. The polycrystalline configuration remained stable at the end of the cooling process at point F (299 K). The PE values of the reheating process followed the same path as the cooling values until point D (513 K), at which the NP remained in the solid phase. Quasi-liquid regions appeared on the left side of the NP at point H (906 K) and completed the melting process at point I (906 K), which is higher than the freezing temperature (470 K) and slightly lower than $T_m$ of the single-crystal NP (977 K). Thermal hysteresis between melting and freezing was also observed in amorphous NPs.[65] We should also add that freezing has occurred over a temperature range and not at one single temperature as in melting. Thus, further work is needed to identify the solidification kinetics of NPs. Bistability below $T_m$, which occurred for smaller Ag NPs, was not observed here for 4 nm particle and larger sizes as well.[66]

Our simulation was performed on single NPs with a free surface and a perfect crystal without defects. Lower $T_m$ values obtained experimentally than values calculated here can be attributed to various possible reasons. Nanoparticles with higher packing factors or with polycrystalline structure should have a lower $T_m$ than an individual single crystal NP. Ag NPs embedded in silica matrix had $T_m$ values in the range of (423 to 623 K) in the size range of (8 to 30 nm).[27] Another work showed $T_m$ values of ~700 K for Ag NPs in the range of (4 to 7 nm), and this was explained by uncontrolled oxidation of the


dx.doi.org/10.1021/jp311541c | J. Phys. Chem. C XXXX, XXX, XXX−XXX

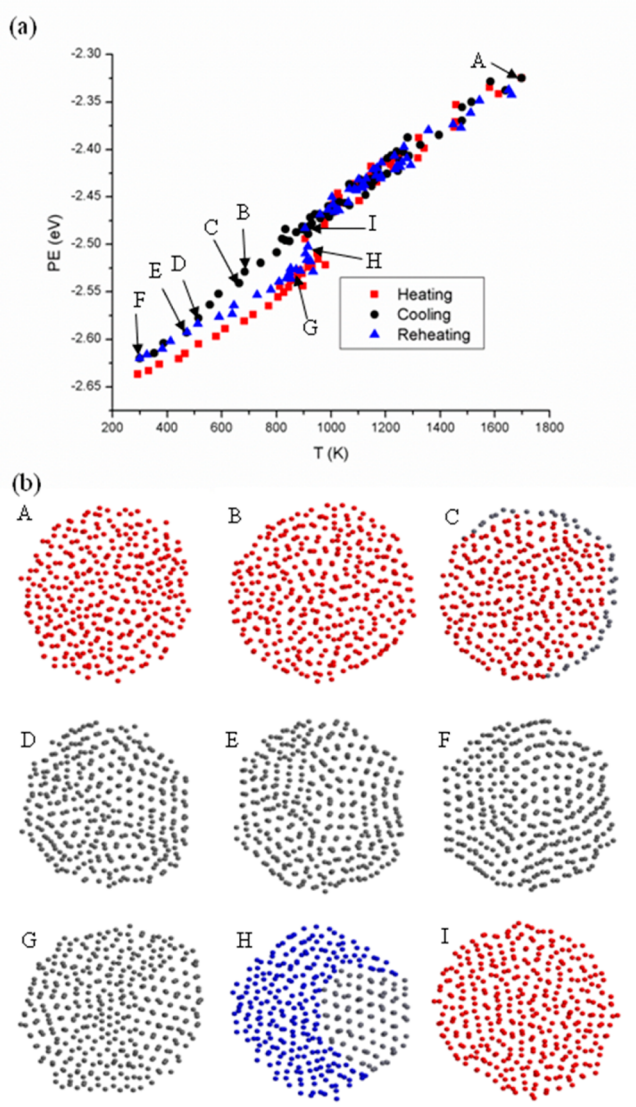


**Figure 10.** (a) Potential energy (PE) values during heating, cooling, reheating of a 4 nm Ag particle. Arrows over the values head toward cooling points while the arrows below the values head toward reheating points. (b) Atomic arrangement of the 6 nm Ag particle at different temperatures shown by letters on the PE curve. Atoms are represented by dots. Each color in the atomic plots represents a phase (gray: solid, blue: quasi-liquid, red: liquid).

NPs.[28] Both effects of embedding matrix and oxidation should increase $T_m$ of the NP due to the reduction of surface energy. However, packing factors or the polycrystalline structure may have had a stronger effect and caused a decreased $T_m$. Other literature also showed very low $T_m$ values of (383 K) for Ag NPs of sizes in the range of 8 to 25 nm[29,30] and 385 to 466 K for sizes in the range of 3.5 to 6.5 nm.[31] It is notable that the onset temperature of thermal sintering is not the complete melting point because solid-state diffusion will also occur.[3] The closest $T_m$ values to those found in our work were obtained for one individual NP studied under TEM with a heating stage and showed values in the range of 773 to 953 K for NPs of sizes in the range of 5 to 50 nm.[32] In that work, the crystalline structure of the examined particles was not determined. An NP that is surrounded by other NPs might also have a much lower $T_{sm}$ value because surface atoms might detach from the NPs and melt during surface diffusion between the NPs.[67] Our previous experimental work showed local surface premelting of 40 nm Ag NPs at 573 K.[68] The reduction of $T_{sm}$ in our previous experimental work might also be due to the NP crystalline structure and packing factor.

We should also point out that our results are based on the heating rate specified in this study. Figure 11 shows PE values

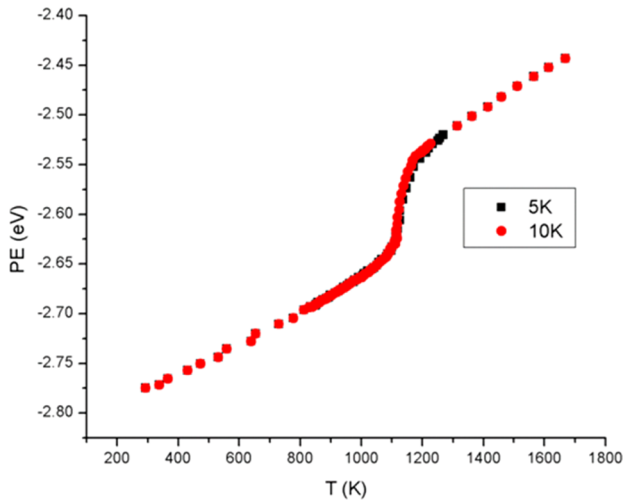


**Figure 11.** Potential energy (PE) values during heating of 4 nm Ag particle at two different temperature steps in temperature regime of (825 to 1275 K).

of heating of 18 nm particle with a 5 K temperature step between 825 and 1275 K compared with the original heating rate of 10 K temperature steps in the same temperature regime. The slower heating rate did not affect the $T_{sm}$ value but reduces the $T_m$ value from 1250 to 1210 K. Thus, superheating of the 18 nm particle occurred due to the heating rate used in this study. For more accurate determination of $T_m$ in future work, slow heating rate, especially in the region between $T_{sm}$ and $T_m$, should be applied.

The many-body EAM used here is the first alternative to the traditional pairwise potentials, which are usually fitted based on the context of bulk properties within ambient conditions. Thus, transferability of pairwise potentials might be problematic for systems containing surfaces and interfaces. This problem is not seen in EAM potentials that account for the energy of an embedded atom in a homogeneous electron gas. Nevertheless, any approach in computer simulation will not reproduce experimental findings unless the same conditions are mimicked. Although, to this fact, we expect to mimic a realistic trend in the studied system for any thermodynamics or structural properties with a well-parametrized many-body potential.[69]

## CONCLUSIONS

Complete melting and surface premelting temperatures of (4 to 20 nm) single-crystal Ag NPs were determined by MD simulation. Our simulation has covered a larger size span than that in previous theoretical models. Hanszen's model was found to be valid for (8 to 10 nm) particles, while Shi's model and liquid drop model were found to be able to predict the melting point of smaller NPs. Unlike previous surface premelting studies that suggested that surface premelting and complete melting occur at one single temperature, melting of NPs in the size range of (8 to 20 nm) occurred at a temperature range and started by forming quasi-liquid ponds on the surface


dx.doi.org/10.1021/jp311541c | J. Phys. Chem. C XXXX, XXX, XXX−XXX

of the NP at a surface premelting temperature ($T_{sm}$). As temperature increased, those quasi-liquid ponds grew and formed a contiguous quasi-liquid layer. As a general rule, the ratio of the quasi-liquid layer thickness to the NP radius showed a linear relationship with temperature. A liquid layer of a critical thickness ($t_o$ = 1.8 nm) was formed once the whole particle had transitioned to the quasi-liquid phase for NPs in the size range of (8 to 10 nm) and once the quasi-liquid layer reached a thickness of 5 nm for larger particles. The liquid layer expanded to complete the melting of the NP at its complete melting temperature ($T_m$). Ag NPs that were smaller than 8 nm melted at a single temperature ($T_m$) without passing through the surface premelting stage. For NPs in the size range of 12 to 20 nm, $T_m$ values deviated from Hanszen's model and approached $T_m$ of the bulk.

## ■ ASSOCIATED CONTENT

### Supporting Information

Initial atomic configurations of the NPs (100) plane after relaxation at 300 K (room temperature). Number of atoms as well as exact complete melting temperatures ($T_m$) and surface premelting temperatures ($T_{sm}$) obtained by our simulations and other analytical models for all simulated sizes of Ag NPs. Fitting parameters of the EAM for Ag. This material is available free of charge via the Internet at http://pubs.acs.org.

## ■ AUTHOR INFORMATION

### Corresponding Author

*E-mail: a2hu@uwaterloo.ca. Phone: (+1)519-8884567x35464. Fax: (+1)519-8886197.

### Notes

The authors declare no competing financial interest.

## ■ ACKNOWLEDGMENTS

This work is partially supported by the National Science and Engineering Research Council of Canada (NSERC). H.A.A. acknowledges the sponsorship of King Abdulaziz City for Science and Technology during this work and also acknowledges that the computations were performed at Çankaya University.

## ■ REFERENCES

(1) Hirose, A.; Kobayashi, K. F. Bonding Using Nanoparticles. In *Microjoining and Nanojoining*; Zhou, Y., Eds; CRC Press/Woodhead Publishing: Cambridge, U.K., 2008; Vol. *I*, pp 250−268.

(2) Alarifi, H.; Hu, A.; Yavuz, M.; Zhou, Y. Silver Nanoparticle Paste for Low-Temperature Bonding of Copper. *J. Electron. Mater.* **2011**, *40*, 1394−1402.

(3) Hu, A.; Guo, J. Y.; Alarifi, H.; Patane, G.; Zhou, Y.; Compagnini, G.; Xu, C. X. Low Temperature Sintering of Ag Nanoparticles for Flexible Electronics. *Appl. Phys. Lett.* **2010**, *97*, 153117−1−3.

(4) Ide, E.; Angata, A.; Hirose, A.; Kobayashi, K. F. Metal-Metal Bonding Process using Ag Metallo-Organic Nanoparticles. *Acta Mater.* **2005**, *53*, 2385−2393.

(5) Allen, G. L.; Bayles, R. A.; Gile, W. W.; Jesser, W. A. Small Particle Melting of Pure Metals. *Thin Solid Films* **1986**, *144*, 297−308.

(6) Dick, K.; Dhanasekaran, T.; Zhang, Z.; Meisel, D. Size-Dependent Melting of Silica-Encapsulated Gold Nanoparticles. *J. Am. Chem. Soc.* **2002**, *124*, 2312−2317.

(7) Güvenc, Z. B.; Jellinek, J.; Voter, A. F. In *Physics and Chemistry of Finite Systems: From Clusters to Crystals*; Jena, P., Khanna, S. N., Rao, B. K., Eds.; Kluwer Academic Publishers: Dordrecht, The Netherlands, 1992; Vol. *I*, p 411.

(8) Yıldırım, E. K.; Atiş, M.; Güvenç, Z. B. Structure and Dynamical Properties of $Au_N$, N = 12−14 Clusters: Molecular Dynamics Simulation. *Int. J. Mod. Phys. C* **2005**, *16*, 99−116.

(9) Böyükata, M.; Güvenç, Z. B. MD Study of Energetics, Melting and Isomerization of Aluminum Microclusters. *Braz. J. Phys.* **2006**, *36*, 720−724.

(10) Kang, K.; Qin, S.; Wang, C. Size-Dependent Melting: Numerical Calculations of the Phonon Spectrum. *Physica E* **2009**, *41*, 817−821.

(11) Mei, Q. S.; Lu, K. Melting and Superheating of Crystalline Solids: From Bulk to Nanocrystals. *Prog. Mater. Sci.* **2007**, *52*, 1175−1262.

(12) Nanda, K. K.; Sahu, S. N.; Behera, S. N. Liquid-Drop Model for the Size-Dependent Melting of Low-Dimensional Systems. *Phys. Rev. A* **2002**, *66*, 013208-1−013208-8.

(13) Shi, F. G. Size Dependent Thermal Vibrations and Melting in Nanocrystals. *J. Mater. Res.* **1994**, *9*, 1307−1313.

(14) Hanszen, K.-J. Theoretische Untersuchungen über den Schmelzpunkt kleiner Kügelchen Ein Beitrag zur Thermodynamik der Grenzflächen. *Z. Phys.* **1960**, *157*, 523−553.

(15) Lereah, Y.; Kofman, R.; Pénisson, J. M.; Deutscher, G.; Cheyssac, P.; Ben David, T.; Bourret, A. Time-Resolved Electron Microscopy Studies of the Structure of Nanoparticles and their Melting. *Philos. Mag. B* **2001**, *81*, 1801−1819.

(16) Pluis, B.; Frenkel, D.; van der Veen, J. F. Surface-Induced Melting and Freezing II. A Semi-Empirical Landau-Type Model. *Surf. Sci.* **1990**, *239*, 282−300.

(17) Bachels, T.; Güntherodt, H.-J.; Schäfer, R. Melting of Isolated Tin Nanoparticles. *Phys. Rev. Lett.* **2000**, *85*, 1250−1253.

(18) Lai, S. L.; Guo, J. Y.; Petrova, V.; Ramanath, G.; Allen, L. H. Size-Dependent Melting Properties of Small Tin Particles: Nanocalorimetric Measurements. *Phys. Res. Lett.* **1996**, *77*, 99−102.

(19) Peters, K. F.; Cohen, J. B.; Chung, Y.-W. Melting of Pb Nanocrystals. *Phys. Rev. B.* **1998**, *57*, 13430−13438.

(20) Wang, Z. L.; Petroski, J. M.; Green, T. C.; El-Sayed, M. A. Shape Transformation and Surface Melting of Cubic and Tetrahedral Platinum Nanocrystals. *J. Phys. Chem. B* **1998**, *102*, 6145−6151.

(21) Wang, N.; Rokhlin, S. I.; Farson, D. F. Nonhomogeneous Surface Premelting of Au Nanoparticles. *Nanotechnology* **2008**, *19*, 415701-1−415701-7.

(22) Hu, W.; Xiao, S.; Yang, J.; Zhang, Z. Melting Evolution and Diffusion Behavior of Vanadium Nanoparticles. *Eur. Phys. J. B* **2005**, *45*, 547−554.

(23) Özdoğan, C.; Erkoç, Ş. Molecular-Dynamics Simulation of the Structural Stability, Energetics, and Melting of $Cu_n$ ($n$ = 13−135) Clusters. *Z. Phys. D* **1997**, *41*, 205−209.

(24) Neyts, E. C.; Bogaerts, A. Numerical Study of the Size-Dependent Melting Mechanisms of Nickel Nanoclusters. *J. Phys. Chem. C* **2009**, *113*, 2771−2776.

(25) Güvenç, Z. B.; Jellinek, J. Surface Melting in $Ni_{55}$. *Z. Phys. D* **1993**, *26*, 304−306.

(26) Chernyshev, A. P. Effect of Nanoparticle Size on the Onset Temperature of Surface Melting. *Mater. Lett.* **2009**, *63*, 1525−1527.

(27) Yeshchenko, O. A.; Dmitruk, I. M.; Alexeenko, A. A.; Kotko, A. V. Surface Plasmon as a Probe for Melting of Silver Nanoparticles. *Nanotechnology* **2010**, *21*, 045203-1−045203-6.

(28) Castro, T.; Reifenberger, R.; Choi, E.; Andres, R. P. Size-Dependent Melting Temperature of Individual Nanometer-Sized Metallic Clusters. *Phys. Rev. B* **1990**, *42*, 8548−8556.

(29) Dong, R.-X.; Chou, C.-C.; Lin, J.-J. Synthesis of Immobilized Silver Nanoparticles on Ionic Silicate Clay and Observed Low-Temperature Melting. *J. Mater. Chem.* **2009**, *19*, 2184−2188.

(30) Chiu, C.-W.; Hong, P.-D.; Lin, J.-J. Clay-Meditated Synthesis of Silver Nanoparticles Exhibiting Low-Temperature Melting. *Langmuir* **2011**, *27*, 11690−11696.

(31) Kim, N. H.; Kim, J.-Y.; Ihn, K. J. Preparation of Silver Nanoparticles Having Low Melting Temperature Through a New Synthetic Process without Solvent. *J. Nanosci. Nanotechnol.* **2007**, *7*, 3805−3809.

(32) Asoro, M. A.; Kovar, D.; Damiano, J.; Ferreira, P. J. Scale Effect on the Melting Behavior of Silver Nanoparticles. *Microsc. Microanal.* **2010**, *16*, 1802−1803.
(33) Atiş, M.; Aktaş, H.; Güvenç, Z. B. Structures and Melting of $Ag_N$ (N = 7, 12−14) Clusters. *Modell. Simul. Mater. Sci. Eng.* **2005**, *13*, 1411−1432.
(34) Atiş, M.; Özdoğan, C.; Güvenç, Z. B. Parallelization of a Molecular Dynamics Simulation of an Ion-Surface Collision System: Ar-Ni (100). *Int. J. Mod. Phys. C* **2005**, *16*, 969−990.
(35) Marks, L. D. Modified Wulff Constructions for Twinned Particles. *J. Cryst. Growth* **1983**, *61*, 556−566.
(36) Voter, A. F. Embedded Atom Method Potentials for Seven FCC metals: Ni, Pd, Pt, Cu, Ag, Au, and Al; Los Alamos Unclassified Technical Report LA-UR 93-3901; Los Alamos National Laboratory: Los Alamos, NM, 1993.
(37) Foiles, S. M.; Baskes, M. I.; Daw, M. S. Embedded-Atom-Method Functions for the FCC Metals Cu, Ag, Au, Ni, Pd, Pt, and their Alloys. *Phys. Rev. B* **1986**, *33*, 7983−7991.
(38) Grigoryan, V. G.; Alamanova, D.; Springborg, M. Structure and Energetics of $Cu_N$ Clusters with ($2 < N < 150$): An Embedded-Atom-Method Study. *Phys. Rev. B* **2006**, *73*, 115415-1−115415-13.
(39) Doye, J. P. K.; Wales, D. J. Global Minima for Transition Metal Clusters Described by Sutton-Chen Potentials. *New J. Chem.* **1998**, *22*, 733−744.
(40) Darby, S.; Mortimer-Jones, T. V.; Johnston, R. L.; Roberts, C. Theoretical Study of Cu-Au Nanoalloy Clusters Using a Genetic Algorithm. *J. Chem. Phys.* **2002**, *116*, 1536−1550.
(41) Finnis, M. W.; Sinclair, J. E. A Simple Empirical *N*-body Potential for Transition Metals. *Philos. Mag. A* **1984**, *50*, 45−55; **1986**, *53*, 161−161.
(42) García-Rodeja, J.; Rey, C.; Gallego, L. J.; Alonso, J. A. Molecular-Dynamics Study of the Structures, Binding Energies, and Melting of Clusters of FCC Transition and Noble metals Using the Voter and Chen Version of the Embedded-Atom Model. *Phys. Rev. B* **1994**, *49*, 8495−8498.
(43) Kuiying, C.; Hongbo, L.; Xiaoping, L.; Qiyong, H.; Zhuangqi, H. Molecular Dynamics Simulation of Local Structure of Aluminium and Copper in Supercooled Liquid and Solid State by Using EAM. *J. Phys.: Condens. Matter* **1995**, *7*, 2379−2394.
(44) Chantasiriwan, S.; Milstein, F. Higher-Order Elasticity of Cubic Metals in the Embedded-Atom Method. *Phys. Rev. B* **1996**, *53*, 14080−14088.
(45) Chantasiriwan, S.; Milstein, F. Embedded-Atom Models of 12 Cubic Metals Incorporating Second- and Third-Order Elastic-Moduli Data. *Phys. Rev. B* **1998**, *58*, 5996−6005.
(46) González, L. G.; Montejano-Carrizales, J. M. Embedded Atom Method Applied to Ni, Cu, Ag, and Pd. *Phys. Status Solidi B* **2000**, *220*, 357−362.
(47) Hansen, L. B.; Stoltze, P.; Nørskov, J. K.; Clausen, B. S.; Niemann, W. Is There a Contraction of the Interatomic Distance in Small Metal Particles? *Phys. Rev. Lett.* **1990**, *64*, 3155−3158.
(48) Valkealahti, S.; Manninen, M. Instability of Cuboctahedral Copper Clusters. *Phys. Rev. B* **1992**, *45*, 9459−9462.
(49) Christensen, O. B.; Jacobsen, K. W. The Coupling Between Atomic and Electronic Structure in Small Cu Clusters. *J. Phys.: Condens. Matter* **1993**, *5*, 5591−5602.
(50) Zhurkin, E. E.; Hou, M. Structural and Thermodynamic Properties of Elemental and Bimetallic Nanoclusters: An Atomic Scale Study. *J. Phys.: Condens. Matter* **2000**, *12*, 6735−6754.
(51) Zhang, T.; Wu, A.-L.; Guan, L.; Qi, Y.-H. Simulations of Metal Cu in Heating Process. *Chin. J. Chem.* **2004**, *22*, 148−151.
(52) Baletto, F.; Ferrando, R.; Fortunelli, A.; Montalenti, F.; Mottet, C. Crossover Among Structural Motifs in Transition and Noble-Metal Clusters. *J. Chem. Phys.* **2002**, *116*, 3856−3863.
(53) Kabir, M.; Mookerjee, A.; Bhattacharya, A. K. Structure and Stability of Copper Clusters: A Tight-Binding Molecular Dynamics Study. *Phys. Rev. A* **2004**, *69*, 043203-1−043203-10.
(54) Schebarchov, D.; Hendy, S. C. Static, Tansient, and Dynamic Phase Coexistence in Metal Nanoclusters. *J. Chem. Phys.* **2005**, *123*, 104701-1−104701-9.
(55) Daw, M. S.; Baskes, M. I. Embedded-Atom Method: Derivation and Application to Impurities, Surfaces, and Other Defects in Metals. *Phys. Rev. B* **1984**, *29*, 6443−6453.
(56) Lindemann, F. A. The Calculation of Molecular Vibration Frequencies. *Phys. Z.* **1910**, *11*, 609−612.
(57) Jiang, Q.; Zhou, X. H.; Zhao, M. Nucleation Temperature of Elements. *J. Chem. Phys.* **2002**, *117*, 10269−10273.
(58) Zhao, S.; Wang, S.; Ye, H. Size-Dependent Melting Properties of Free Silver Nanoclusters. *J. Phys. Soc. Jpn.* **2001**, *70*, 2953−2957.
(59) Chernyshev, A. P. Melting of Surface Layers of Nanoparticles: Landau Model. *Mater. Chem. Phys.* **2008**, *112*, 226−229.
(60) Gupta, R. P. Lattice Relaxation at a Metal Surface. *Phys. Rev. B* **1981**, *23*, 6265−6270.
(61) Skripov, V. P.; Koverda, V. P.; Skokov, V. N. Size Effect on Melting of Small Particles. *Phys. Status Solidi A* **1981**, *66*, 109−118.
(62) Wronski, C. R. M. The Size Dependence of the Melting Point of Small Particles of Tin. *Brit. J. Appl. Phys.* **1967**, *18*, 1731−1737.
(63) Alymov, M. I.; Maltina, E. I.; Stepanov, Y. N. Model of Initial Stage of Ultrafine Metal Powder Sintering. *Nanostruct. Mater.* **1994**, *4*, 737−742.
(64) Garrigos, R.; Cheyssac, P.; Kofman, R. Melting for Lead Particles of Very Small Sizes; Influence of Surface Phenomena. *Z. Phys. D* **1989**, *12*, 497−500.
(65) Hoang, V. V. Melting of Simple Monoatomic Amorphous Nanoparticles. *J. Phys. Chem. C* **2012**, *116*, 14728−14735.
(66) Zhao, S. J.; Wang, S. Q.; Cheng, D. Y.; Ye, H. Q. Three Distinctive Melting Mechanisms in Isolated Nanoparticles. *J. Phys. Chem. B* **2001**, *105*, 12857−12860.
(67) Karabacak, T.; DeLuca, J. S.; Wang, P.-I.; Eyck, G. A. T.; Ye, D.; Wang, G.-C.; Lu, T. M. Low Temperature Melting of Copper Nanorod Arrays. *J. Appl. Phys.* **2006**, *99*, 064304-1−064304-6.
(68) Alarifi, H.; Hu, A.; Yavuz, M.; Zhou, Y. Pressureless Sintering Behavior of Silver Nanoparticles at Low Temperatures. *Mater. Sci. Technol.* **2010**, *4*, 2633−2641.
(69) Foiles, S. M.; Baskes, M. I. Contributions of the Embedded-Atom Method to Materials Science and Engineering. *MRS Bull.* **2012**, *37*, 485−491.